MgO nanostructure via a sol–gel combustion synthesis method using different fuels: An efficient nano-adsorbent for the…

Article *in* Journal of Molecular Liquids · November 2016

DOI: 10.1016/j.molliq.2016.10.135

CITATIONS
15

READS
117

4 authors, including:

Mostafa Y Nassar
Benha University
42 PUBLICATIONS **434** CITATIONS
SEE PROFILE

Ibrahim S Ahmed
Benha University
50 PUBLICATIONS **477** CITATIONS
SEE PROFILE

Journal of Molecular Liquids 225 (2017) 730–740

Contents lists available at ScienceDirect

Journal of Molecular Liquids

journal homepage: www.elsevier.com/locate/molliq

MgO nanostructure via a sol-gel combustion synthesis method using different fuels: An efficient nano-adsorbent for the removal of some anionic textile dyes

Mostafa Y. Nassar *, Talaat Y. Mohamed *, Ibrahim S. Ahmed, Ihab Samir

Chemistry Department, Faculty of Science, Benha University, Benha 13518, Egypt

ARTICLE INFO

Article history:
Received 28 June 2016
Received in revised form 20 September 2016
Accepted 31 October 2016
Available online 2 November 2016

Keywords:
Magnesium oxide nanostructures
Textile dyes
Adsorption
Sol-gel combustion kinetics
Thermodynamics

ABSTRACT

Magnesium oxide nanostructures were synthesized via a sol-gel combustion method using urea, oxalic acid, and citric acid fuels. The effect of the fuel type on the products was studied. The as-prepared products were characterized by means of FE-SEM, HR-TEM, XRD, and FT-IR analyses. The results exhibited that the used fuels gave MgO products with different morphologies, and the oxalic acid fuel produced pure MgO nanoparticles with the smallest crystallite size (ca. 12 nm). The adsorption properties of the MgO products for the removal of Reactive Red 195 (RR195) and Orange G (OG) anionic dyes were examined. Using a batch method, various parameters affecting the adsorption properties were studied. The results revealed that MgO nanostructure generated from the oxalic acid fuel had the highest adsorption capacities (207 and 21.5 mg/g for RR195 and OG dyes, respectively). Additionally, the adsorption data followed the pseudo-second-order kinetic model and Langmuir adsorption isotherm model. And the adsorption process was controlled by intra-particle diffusion, bulk diffusion, and film diffusion mechanisms. Besides, the thermodynamic study showed that the adsorption of the textile dyes of interest on the as-prepared MgO nanostructures was an exothermic, physisorption and spontaneous process.

1. Introduction

Recently, much consideration has been paid to the environment to keep it free from the textile dye contaminations [1–4]. The discharged wastewater of the textile industries contains unavoidable byproducts as a result of the dyeing process. It is assessed that around 1–20% of dyes are discharged into the environment upon completion the dyeing process, and about 125–150 L of water is employed for each 1 kg of the textile product [5–7]. Among these dyes are the reactive dyes which are extensively utilized in textile industries due to their strong interaction with the natural and synthetic fabrics surfaces [8]. However, releasing this kind of dyes including Orange G (OG) and Reactive Red 195 (RR195) dyes into the aquatic environment results in various problematic issues such as undesirable colors, inhibition the sunlight penetration into the aquatic media, as well as toxicity and carcinogenicity of these dyes [2,9]. Hence, removing dyes from wastewater and its treatment is economically and environmentally of great importance.

In this vein, various conventionally biological, physical and chemical methods have been proposed to get rid of synthetic and natural dyes from wastewaters such as sedimentation, activated sludge, membrane separation, coagulation, ozonation, photocatalytic degradation, adsorption, electrochemical and ultrasonic techniques, fungal, decolorization aerobic and anaerobic microbial degradation, etc. [10–15]. It is notable that most of these methods have one or more drawbacks in wastewater treatment; however, on the other hand, adsorption method still has the superiority over all methods due to its simplicity, high efficiency, cheapness, and regeneration of the adsorbents. Therefore, various adsorbents have been suggested for treatment of wastewaters from dyes, such as clays, sagaun sawdust, activated carbons alginate, natural and synthetic polymers, surfactant-modified natural zeolite, and hydrotalcites [1,16–19].

Recently, a considerable attention has been paid to utilizing nanomaterials, including metal oxides, as nano-adsorbents for decontamination of wastewaters because of their high surface area, large numbers of active sites, and high stability [20–28]. Among different nano-adsorbents, nano-sized magnesium oxide (MgO) has received a significant consideration for decontamination of wastewater attributable to its lower cost, chemical stability, non-toxicity, simple production, large surface area, and a high point of zero charge value (12.4) [13,29]. These characteristics support MgO nanoparticles to be employed as a promising candidate for the removal of anionic dyes [29]. Owing to the excellent optical, electrical, thermodynamic, mechanical, electronic, and special chemical properties of MgO nanostructures, they are utilized in various applications including catalysts,

* Corresponding authors.
E-mail addresses: m_y_nassar@yahoo.com, m_y_nassar@fsc.bu.eg.edu (M.Y. Nassar), dr_talaat2003@yahoo.com (T.Y. Mohamed).

http://dx.doi.org/10.1016/j.molliq.2016.10.135
0167-7322/

adsorbents, optoelectronic materials, transparent fillers, antibacterial agents, fire retardants, and electrochemical biosensors [13,30–34]. Therefore, many synthetic methods have been adopted for the preparation of MgO nanoparticles such as laser vaporization, precipitation, hydrothermal, precipitation, sol-gel, combustion, micro-emulsion, chemical gas phase deposition, and laser vaporization technique [13, 35–39]. However, due to the scalability, feasibility, and low-cost of the combustion process, this synthesis route has aroused the interests of many research groups. Moreover, reports on the synthesis of MgO nanoparticles via a combustion or sol-gel combustion route are still limited [36,40].

Herein, we have reported the combustion synthesis of magnesium oxide nanoparticles using inexpensive fuels such as citric acid, oxalic acid, and urea. Removal of some textile dyes such as Reactive Red 195 (RR195) and Orange G (OG) dyes using the as-prepared MgO nanostructures has been extensively investigated. Various experimental factors influencing the adsorption process along with the isotherm models, kinetics, and thermodynamic investigation have been examined.

2. Experimental

2.1. Materials and reagents

All chemicals were of analytical grade and utilized as received without further purification: The chemicals: magnesium nitrate ($Mg(NO_3)_2 \cdot {}_6H_2O$), citric acid ($HOC(COOH) \cdot (CH_2COOH)_2$), oxalic acid ($C_2H_2O_4 \cdot 2H_2O$), and urea ($NH_2CONH_2$) and Orange G dye (OG; $C_{18}H_{10}N_2O_7Na_2$; Scheme 1), were purchased from Sigma-Aldrich Chemical Company. Ammonium hydroxide solution (33%) was supplied by El Nasr Pharmaceutical Chemicals Company (Adwic) Company, Egypt. Reactive Red 195 dye (RR195; $C_{31}H_{19}ClN_7O_{19}S_6Na_5$; Scheme 1) was obtained from Rushabh chemicals industries, India.

2.2. Preparation of MgO nanostructures

Magnesium oxide nanostructures were synthesized via a hybrid sol-gel combustion method in which urea, oxalic acid, and citric acid were used as fuels, and the produced MgO products were referred to as A, B, and C, respectively. In this method, the calculated stoichiometry of the used redox mixture for the combustion process is based on the condition that the equivalence ratio, Φ_c, should be unity (i.e. $\Phi_c = (F/O) = 1$) in order to maximize the released energy from the combustion process for each reaction; where, (O) is the total oxidizing valence of the oxidizer (i.e. magnesium nitrate) and (F) the total reducing valence of the fuel [41]. In a typical preparation procedure: urea aqueous solution (2.0 g, 33.33 mmol, 30 mL) was added to a stirring magnesium nitrate aqueous solution (5.12, 19.97 mmol, 40 mL) set up at ~70 °C. The reaction blend was allowed to stir at 70 °C until it gave a viscous liquid. Afterwards, the temperature was raised to 350 °C, while the entire combustion was achieved in ca. 8 min. The burned precursor was ground and calcined for 2 h at 550 and 800 °C to produce MgO products labeled as A_{550} and A_{800}, respectively. Using similar procedure, magnesium oxide nanoparticles (labeled as B and C) were also synthesized by employing oxalic and citric acids as fuels, respectively. However, ammonium hydroxide solution (2 M) was added to the reaction blend directly after mixing the reactants in these cases. Similarly, the burned precursors were calcined at 550 and 800 °C to give MgO nanostructures referred to as (B_{550}, and B_{800}) and (C_{550}, and C_{800}) in the case of oxalic acid and citric acid fuels, respectively.

2.3. Adsorption experiment

In Erlenmeyer flasks, adsorption investigations were performed by stirring 0.05 mg of MgO nanoparticles in aqueous solutions (25 mL) of RR195 and OG dyes, separately, at room temperature (25 °C). At pre-defined time intervals, aliquots were taken out of the flasks, and centrifuged at 4000 rpm. The concentration of the remaining dye in the supernatant was estimated using the UV–Vis spectrophotometer at the corresponding maximum wavelength of the dyes utilizing their pre-constructed calibration curves. Using Eq. (1), one can calculate the adsorption capacity of the adsorbent (q_t, mg/g); where, C_0 (mg/L) is the initial dye concentration, C_t (mg/L) is the dye concentration in solution at a pre-defined time t, V (L) is the volume of the dye solution, and m (g) is the mass of the magnesium oxide adsorbent. Moreover, Eq. (2) can be employed to estimate the percent removal efficiency (%R) of the dye; where, C_0 and C_t have the previously mentioned meaning.

$$q_t = \frac{V(C_0 - C_t)}{m} \tag{1}$$

$$R = \frac{(C_0 - C_t)}{C_0} \times 100 \tag{2}$$

During this study, various factors have been investigated such as contact time (5–120 min), pH (2–9), KCl concentration (0.05–0.55 g), temperature (298–318 K), and initial dye concentration of 50–700 mg/L for RR195 dye and 10–100 mg for OG dye. Additionally, by utilizing Eq. (3), the equilibrium adsorption capacity of the MgO adsorbent, q_e (mg/g), can be determined.

$$q_e = \frac{V(C_0 - C_e)}{m} \tag{3}$$

where, C_e (mg/L) is the dye concentration at equilibrium in the supernatant after separation of the adsorbent; and V, m, as well as C_0 have the aforementioned meaning.

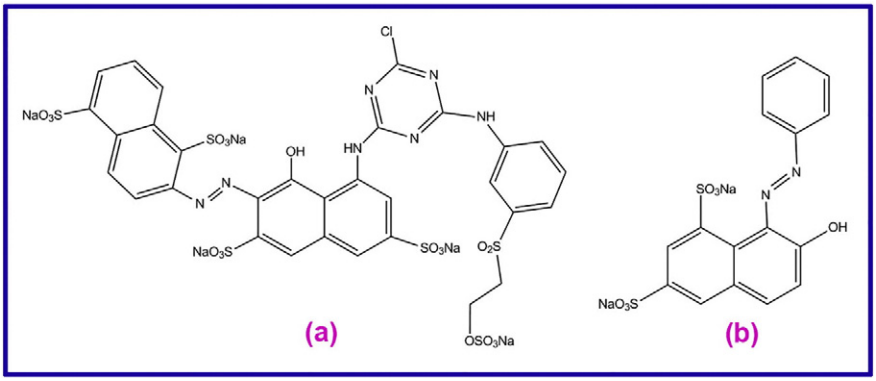

Scheme 1. Chemical structures of Reactive Red 195 (a) and Orange G (b) dyes.

(a) Urea Fuel:

$$6Mg(NO_3)_2.6H_2O(aq) + 10CO(NH_2)_2(aq) \longrightarrow 6MgO(s) + 13N_2(g) + 10CO_2(g) + 38H_2O(g) \quad (4)$$

(b) Oxalic acid Fuel:

$$2Mg(NO_3)_2.6H_2O(aq) + 10C_2H_2O_4.2H_2O \longrightarrow 2MgO(s) + 2N_2(g) + 20CO_2(g) + 42H_2O(g) \quad (5)$$

(c) Citric acid Fuel:

$$18Mg(NO_3)_2.6H_2O(aq) + 10C_6H_8O_7 \longrightarrow 18MgO(s) + 18N_2(g) + 60CO_2(g) + 148H_2O(g) \quad (6)$$

Scheme 2. The proposed combustion reactions of magnesium nitrate with urea, oxalic acid, and citric acid fuels.

2.4. Physico-chemical measurements

Powder X-ray diffraction (XRD) of the samples was collected utilizing an 18 kW diffractometer (Bruker; model D8 Advance) with monochromatic Cu-Kα radiation (λ = 1.54178 Å). FE-SEM images were recorded employing a field emission scanning electron microscope (FE-SEM) with a microscope (JEOL JSM-6500F). The HR-TEM images were collected utilizing a transmission electron microscope (TEM-2100) at a speeding voltage of 200 kV by dispersing the samples in ethanol on a copper grid. FT-IR spectra were recorded using FT-IR spectrometer (Bomem; model MB157S) in the range of 4000–400 cm^{-1} at room temperature. The adsorption investigation was achieved utilizing a UV–Vis spectrophotometer (Jasco; model v530).

3. Results and discussion

3.1. Synthesis and characterization of MgO nanostructures

MgO nanostructures were prepared via a sol-gel combustion method utilizing magnesium nitrate and different fuels such as urea, oxalic acid, and citric acid using fuel-to-oxidant relative ratio (Φ) of 0.6, 0.2 and 1.8, respectively. In this investigation, the type of the fuel has a remarkable influence on the crystallite size and morphology of the MgO products as it will be explained shortly. The proposed combustion reactions of magnesium nitrate and the fuels of interest can be presented by equations 4–6 (Scheme 2). Scheme 2 shows that the molar ratios of Mg^{2+}:urea, Mg^{2+}:oxalic acid, and Mg^{2+}:citric acid are 0.6:1, 0.2:1, and 1.8:1, respectively. The burned and calcined products were characterized using different techniques.

3.1.1. XRD analysis

XRD was employed to investigate the phase composition of the as-prepared MgO nanostructures. Fig. 1 exhibits the XRD patterns of the calcined products at 550 °C. It is clearly seen that 550 °C is enough temperature for urea and oxalic acid fuels to produce pure MgO nanoparticles because all the reflections of their products are indexed well to the cubic phase of MgO (periclase) [JCPDS No. 87-0652; space group: Fm^3m], as shown in Fig. 1(a) and (b), respectively. No other reflections for impurities have been observed. Additionally, the calculated crystallite size (D, nm) for MgO products; A_{550} and B_{550}, was found to be 30 and 12 nm, respectively, using the Debye-Scherrer equation (Eq. (7)) [26,42].

$$D = 0.9\lambda/\beta \cos\theta_B \quad (7)$$

where, λ (nm) is the X-ray radiation wavelength, β is the diffraction peak full width at half maximum (FWHM), and θ_B is the Bragg diffraction angle. Interestingly, it is obvious that using oxalic acid fuel produced MgO nanoparticles with smaller crystallite size on comparing to urea fuel. On the other hand, citric acid fuel did not produce pure MgO nanostructure on combustion, and it generated impure MgO product, C_{550}, even after calcination at 550 °C (Fig. 1(c)). Consequently, it was necessary to increase the calcination temperature to 800 °C for all samples to investigate its influence on the combustion products of the three fuels. Fig. 2(a-c) presented the XRD patterns of the calcined products at 800 °C. It is clearly observed from Fig. 2(c) that 800 °C calcination temperature was enough to generate pure MgO nanostructure (C_{800}) of periclase phase [JCPDS No. 87-0652; space group: Fm^3m] when citric acid was used as a fuel, and the estimated crystallite size was found to be 79 nm. From the other side, increasing the calcination temperature resulted in enhancing the crystallinity of the products generated using oxalic acid and urea fuels; B_{800} and A_{800}, and it reached 51 and 90 nm, respectively. Therefore, it can be concluded that oxalic acid is the optimum fuel in our study because it produces pure MgO nanostructure with the smallest crystallite size at lower temperature (550 °C).

3.1.2. FT-IR analysis

The chemical compositions of the calcined products at 800 °C were further identified using the FT-IR spectra (Fig. 3(a-c)), and the spectra of all products were similar. The FT-IR spectra of the products exhibit

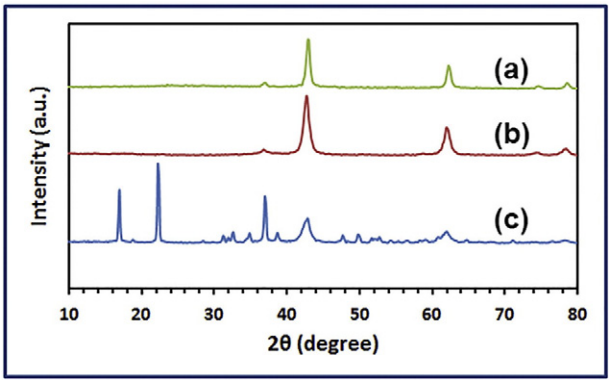

Fig. 1. XRD patterns of the as-prepared MgO products calcined at 550 °C using urea (a), oxalic acid (b), and citric acid (c) fuels.

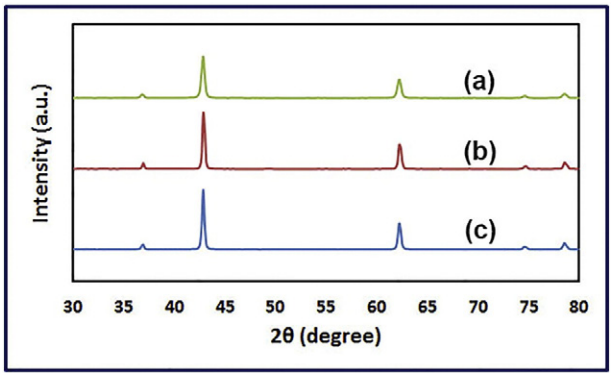

Fig. 2. XRD patterns of the as-prepared MgO products calcined at 800 °C, using urea (a), oxalic acid (b), and citric acid (c) fuels.

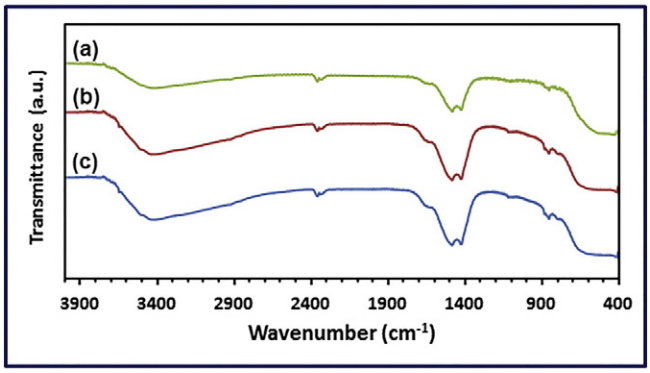

Fig. 3. FT-IR spectra of the as-prepared MgO nanostructures calcined at 800 °C, using urea (a), oxalic acid (b), and citric acid (c) fuels.

vibrational absorptions at 440–700 cm^{-1} which may be assigned to the stretching vibrations of Mg—O. The bands appeared at 840–900 cm^{-1} may be due to stretching vibrations, υ_1 and υ_2, of the magnesium oxygen bond. Finally, the bands appeared at 3290–3650 and 1598–1600 cm^{-1} can be attributed to the stretching and bending vibrational frequencies of the hydroxyl groups of the surface adsorbed waters [15,23,43]. All these data are compatible with those reported by Dhal et al. [38].

3.1.3. Morphology investigation of MgO nanoparticles

Morphologies of the as-prepared MgO products calcined at 800 °C (A_{800}, B_{800}, and C_{800}) have been investigated using field emission scanning electron microscopy (FE-SEM) and high-resolution transmission electron microscopy, as shown in Figs. (4) and (5), respectively. Fig. 4 shows the FE-SEM micrographs of the samples: A_{800}, B_{800}, and C_{800}, and the images reveal that the obtained products are composed of aggregates of flower-like structures. However, when urea was used as fuel, the product (A_{800}) consisted of a flower-like structure composed of plates with an average size of ca. 1.5 μm covered with fine cotton-like structures. On the other hand, when oxalic acid and citric acid fuels were used the flower-like structure products (B_{800} and C_{800}) were composed of plates with an average size of ca. 2 and 1 μm, respectively, which were not covered with cotton-like structures. Notably, producing of MgO products with different morphologies might be due to that the employed fuels in the synthesis procedure produced different quantities of heat and gases during the combustion step which resulted in different morphologies and different crystallite sizes. Further investigation of the morphology of the products using high-resolution transmission electron microscopy (Fig. 5) exhibits that the products;

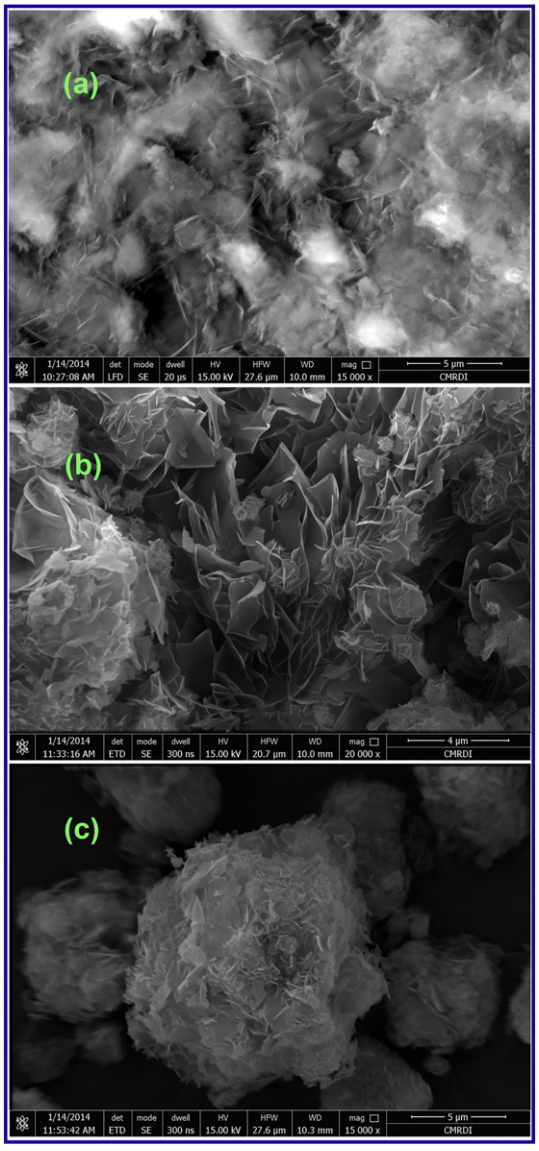

Fig. 4. FE-SEM images of the as-prepared MgO nanostructures calcined at 800 °C, using urea (a), oxalic acid (b), and citric acid (c) fuels.

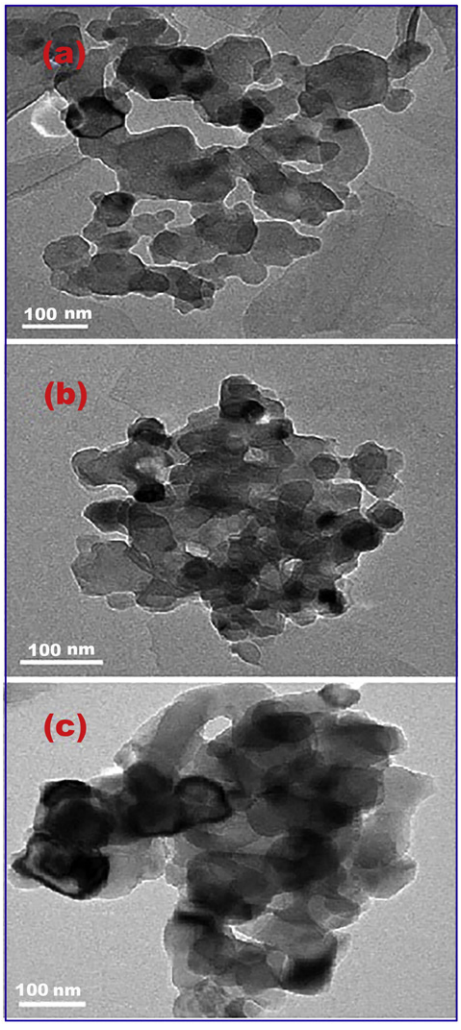

Fig. 5. HR-TEM images of the as-prepared MgO nanostructures calcined at 800 °C, using urea (a), oxalic acid (b), and citric acid (c) fuels.

A_{800}, B_{800}, and C_{800}, are composed of irregular, hexagonal, cubic and spherical shape particles with average diameters of 89, 53, and 81 nm, respectively. These results are compatible with those deduced from XRD data.

3.2. Adsorption studies on MgO nano-adsorbent

We have studied extensively the adsorption of RR195 and OG dyes on the as-prepared MgO nanoparticles (B_{800}) produced using the oxalic acid fuel. Then, the adsorption capacities of the MgO products synthesized using different fuels and calcined at different temperatures were compared as it will be discussed briefly.

3.2.1. Effect of pH

Due to the significant influence of the pH of the adsorption media on the efficiency of the adsorption process, we have investigated the influence of the initial pH of the solution on the removal efficiency of RR195 and OG dyes using MgO nanoparticles under the adsorption conditions: 2–9 pH range, 24 h stirring time, and 0.05 g adsorbent dose. The results are depicted in Fig. 6. The experimental data reveal that the dye removal efficiencies are low at low pH values for both dyes. Moreover, as the pH value increases the dye removal efficiency enhances until it reaches its maximum at pH 4 and 7 for the OG ($\%R = 70\%$) and RR195 ($\%R = 84.4\%$) dyes, respectively. Consequently, the pH values of 4 and 7 are the optimum pH values for the adsorption of OG and RR195 dyes, respectively. Afterward, the removal efficiency reduces slowly for the OG dye or reduces sharply for the RR195 dye on increasing the pH values. This behavior can be explained by taking into the account the surface charge of the MgO nanoparticles and the dye molecules at different pH values. At lower pH values, the particle adsorbent surfaces (hydrous oxide (MOH)) will be probably covered by protons forming positively charged particles ($MOH^{+}{}_{2}$). However, at higher pH values, the hydrous oxide may react with the highly concentrated hydroxide ions to generate negatively charged deprotonated oxide (MO^{-}), as reported by Nassar and others [44–46]. Additionally, since the utilized dyes are anionic dyes (i.e. negatively charged molecules) and the point of zero charge for MgO is ca. 12.4 [13,29], it can be concluded that the adsorption process is mainly controlled by the electrostatic interactions between the negatively charged dye molecules and the charged adsorbent particles. Hence, there will be an attraction between the oppositely charged species at lower pH values and this results in an enhanced adsorption [47]. On the other hand, the smaller value of the adsorption efficiency at higher pH values may be due to the fact that at these pH values there will be a competition between the negatively charged dye molecules and the highly concentrated OH^{-} ions [47,48].

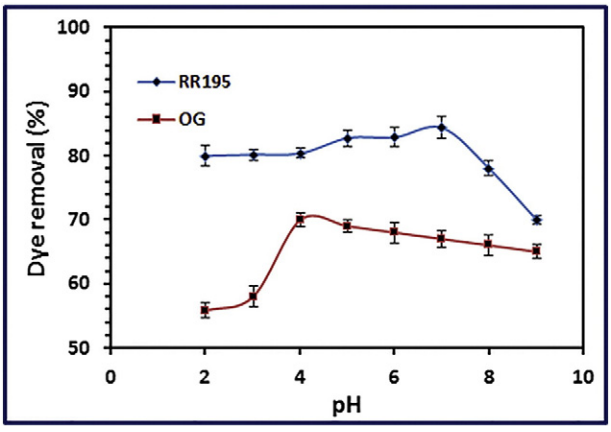

Fig. 6. Effect of pH on the removal of RR195 and OG dyes.

3.2.2. Effect of contact time

The influence of contact time on the adsorption efficiency of MgO nano-adsorbent was studied at pH 4 and pH 7 for OG and RR195 dyes, respectively, using 0.05 g MgO nano-adsorbent and initial dye concentration of 50 and 400 mg/L for OG and RR195 dye, respectively. Fig. 7 displays the dye removal efficiency against stirring time in the range from 5 to 120 min. Inspection of Fig. 7 revealed that the adsorption capacity of MgO adsorbent for the removal of the dyes increased rapidly until it reached ca. 168 and 16.4 mg/g for RR195 and OG dyes, respectively, in 60 min, and it remained constant for 20 min under continued stirring, then decreased. Hence, the optimum contact time for the dyes was chosen to be 60 min because the adsorption process reached the equilibrium at that time and remained constant for some time. However, the decrease in the dye removal efficiency at 80 min may be due to the increase in temperature of the adsorption medium to a few degrees because of the frictions and collisions between adsorbent molecules, and as will be seen shortly that this adsorption process is an exothermic process.

3.2.3. Effect of temperature

The temperature of the adsorption medium influences the adsorption process significantly, so that we have investigated the effect of the temperature (25, 35, and 45 °C) on the adsorption of the dyes under study. The adsorption conditions were 0.05 g of the nano-sized MgO and initial dye concentrations of 400 and 50 mg/L for RR195 and OG dyes, respectively. The experimental results revealed that the adsorption efficiency reduces slowly with raising the solution temperature for both dyes as displayed in Fig. 8. Hence, the experimental results indicate that the adsorption of RR195 and OG dyes on MgO nano-adsorbent is an exothermic process. And the reduction in the adsorption rate on raising the temperature may be due to that the dye molecules

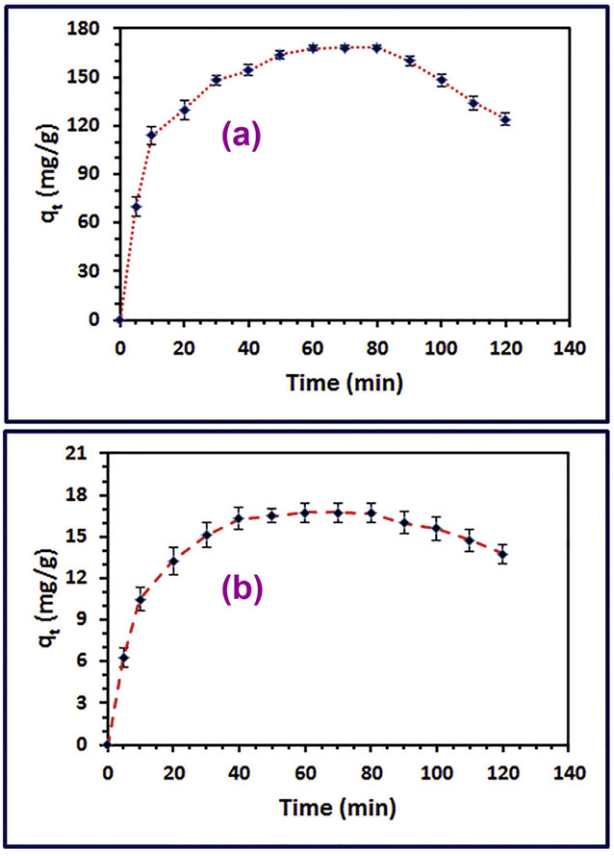

Fig. 7. Effect of the contact time on adsorption of RR195 dye (a) and OG dye (b) on MgO nano-adsorbent.

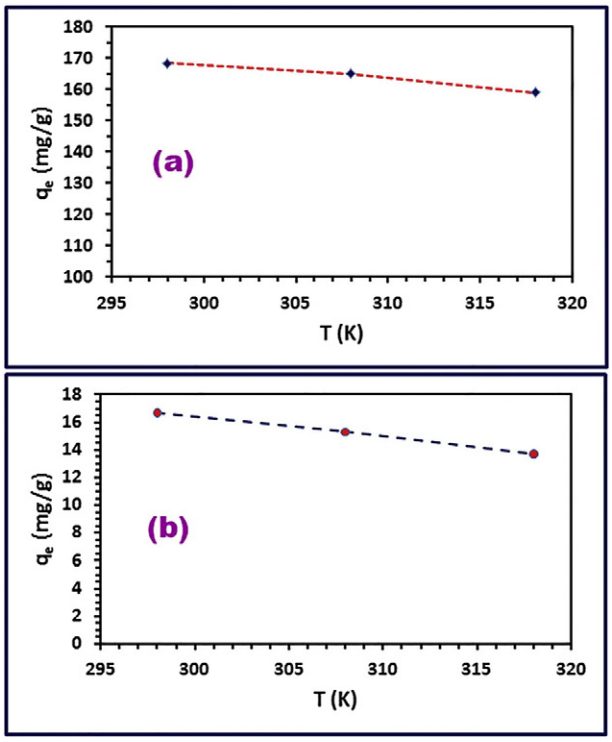

Fig. 8. Effect of temperature on adsorption of RR195 dye (a) and OG dye (b) on MgO nano-adsorbent.

tend to leave the solid phase and escape to liquid phase at higher temperatures [49].

3.2.4. Effect of ionic strength

The effect of ionic strength on the adsorption of the dyes under study on MgO nano-adsorbent was studied utilizing KCl salt of doses ranging from 0.05 to 0.55 g. The results (shown in Fig. 9) reveal that increasing the ionic strength enhances the RR195 dye removal efficiency and decreases the OG dye removal efficiency. This can be attributed to the ionic strength of the adsorption media that can control both electrostatic and non-electrostatic interactions which can exist between the dye molecules and the adsorbent surface. It is known that, theoretically, when there is an electrostatic attraction between the dye molecules and the adsorbent surface, the increase in the ionic strength will result in a reduction in the adsorption capacity; consequently, the adsorption of OG dye on MgO nano-adsorbent follows this convention [44]. However, adsorption of RR195 did not obey this rule and the increase in the dye removal efficiency might be due to dimerization of RR195 dye molecules in solution at higher KCl concentrations. Moreover this aggregation might occur due to increasing in the dipole–dipole, ion-dipole, and van der Waals forces between the dye molecules in solution [44,50].

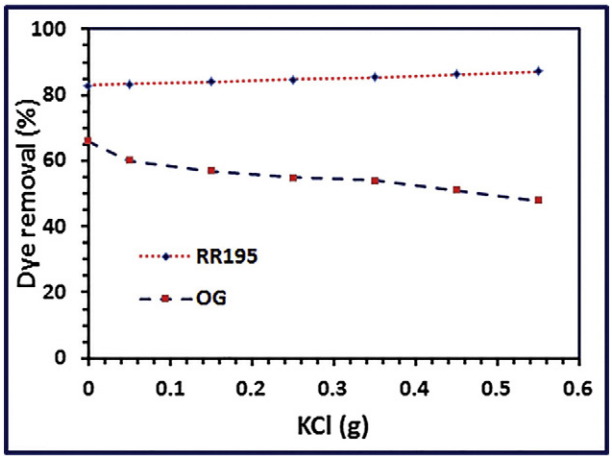

Fig. 9. Influence of KCl concentration on the removal of the removal of RR195 and OG dyes.

3.2.5. Effect of initial dye concentration

The influence of the initial dye concentrations on the adsorption capacity has been investigated in the dye concentration range of 50–700 mg/L and 10–100 mg/L for RR195 and OG dyes, respectively, at 25 °C, utilizing 0.05 g MgO adsorbent. The results are displayed in Fig. 10 (a) and (b), respectively. The experimental data revealed that the adsorption capacity enhanced with increasing the initial dye concentration until it reached saturation at ca. 500 and 60 mg/L, for RR195 and OG dyes, respectively. And the relevant experimental adsorption capacities were found to be 186 and 18.1 mg/g for the aforementioned dyes, respectively. The increase in the adsorption capacity with increasing the initial dye concentration may be due to enhancing the driving forces to overwhelm the resistance of the mass transfer of the dye molecules between the liquid phase and the solid phase during the adsorption process [51].

3.2.6. Adsorption kinetics studies

Studying the adsorption kinetics is an important factor because this study can be employed to predict the adsorption mechanism and the removal rate of the dyes of interest. This kind of investigation helps also to design a practical system for water treatment from pollutants. In this vein, the kinetic results were examined using the pseudo-first-order (Eq. (8)), pseudo-second-order (Eq. (9)), and intra-particle diffusion (Eq. (10)) models in their linearized forms [2,3,23,52].

$$\log(q_e - q_t) = \log q_e - \frac{k_1}{2.303} t \tag{8}$$

$$\frac{t}{q_t} = \frac{1}{k_2 q_e^2} + \frac{t}{q_e} \tag{9}$$

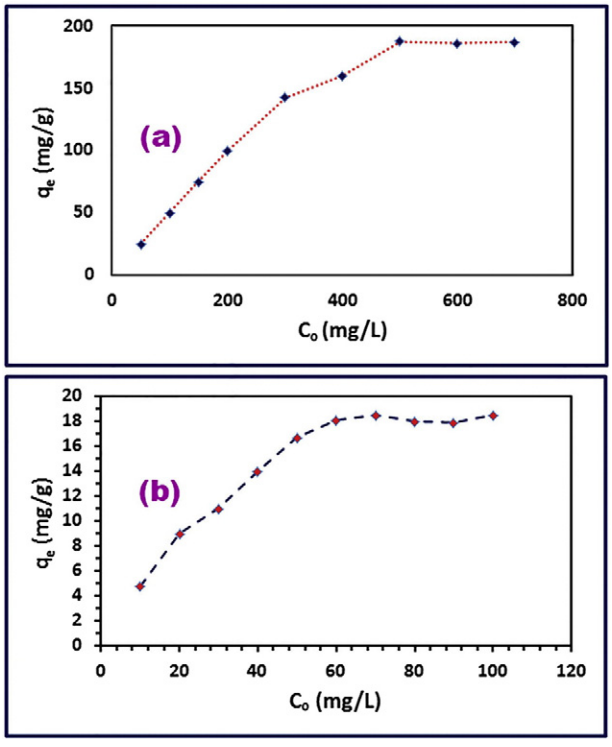

Fig. 10. Influence of initial dye concentration on adsorption of RR195 dye (a) and OG dye (b) on MgO nano-adsorbent.

Table 1
Kinetic constants for the adsorption of RR195 and OG dyes on MgO adsorbent.

Kinetics models	Constants	RR195 dye Value	OG dye Value
Pseudo-first-order	K_1 (1/min)	0.128	0.112
	$q_{e(cal)}$ (mg/g)	22,793	16.4
	r_1^2	0.49	0.65
	$q_{e(exp)}$ (mg/g)	168.4	16.7
Pseudo-second-order	K_2 [g/(mg min)]	0.0007	0.0066
	$q_{e(cal)}$ (mg/g)	186.4	18.8
	r_2^2	0.999	0.998
	$q_{e,exp.}$ (mg/g)	168.4	16.7
	h(mg/g min)	24.24	2.34

$$q_t = k_i t^{0.5} + C \quad (10)$$

where, q_e is the quantity of the adsorbed dye at equilibrium (mg/g), q_t (mg/g) is the quantity of the adsorbed dye at time t (min), k_1 is the pseudo-first-order rate constant of the adsorption process (1/min), k_2 is the pseudo-second-order rate constant of the adsorption process (g/(mg.min)), C is the intercept (mg/g) for Eq. (10) which indicates the thickness of the boundary layer, and k_i is intra-particle diffusion rate constant (mg/(g.min$^{0.5}$)). The estimated kinetic constants after applying the models 8 through 10 for the adsorption process are presented in Table 1. Eq. (8) was applied to estimate the pseudo-first-order rate constant and the other related constants, as presented in Table 1, by drawing log(q_e-q_t) against t (results are not displayed). Plus, plotting t/q_t versus t results in a straight line (Fig. 11(b,c)), and from the slope and intercept of the line the constants of the pseudo-second-order model are calculated and tabulated in Table 1. It is noticed that the adsorption of RR195 and OG dyes on the MgO adsorbent obeys pseudo-second-order model, as it is clear from the values of the correlation coefficients (r^2) which are close to unity on comparing with those obtained from the pseudo-first-order model for both dyes. Furthermore, this conclusion is supported by the values of the calculated adsorption capacities ($q_{e(cal)}$). It is found (as presented in Table 1) that the calculated values employing the pseudo-second-order model for both dyes are much more closer to the experimentally obtained ones ($q_{e(exp)}$) on comparing to those calculated from the pseudo-first-order model. Consequently, the initial sorption rate (h) based on the pseudo-second-order rate model was calculated employing Eq. (11) and presented in Table 1 [53].

$$h = k_2 q_e^2 \quad (11)$$

To investigate the adsorption mechanism of the rate determining step of the adsorption process, Weber-Morris intra-particle diffusion model (Eq. (10)) was utilized to examine the adsorption data. This is achieved by plotting q_t versus $t^{0.5}$, as shown in Fig. 11(c) and (d) for the adsorption of RR195 and OG dyes, respectively. The plots do not pass the origin and reveal a three-stage linearity, and this indicates that the rate determining step of adsorption of the dyes on MgO adsorbent is not only controlled by an intra-particle diffusion mechanism but also controlled by some other mechanisms including bulk diffusion and film diffusion [54].

3.2.7. Adsorption isotherms study

Adsorption isotherms deal with the relationships between the concentration of the adsorbate (C_e) in the liquid phase and its concentration on the adsorbent at equilibrium and constant temperature [55]. The collected adsorption data were examined employing two well-known adsorption isotherms such as Langmuir and Freundlich isotherm models, to gain further information on the adsorption mechanism of the dyes under study. Formation of a monolayer adsorbate where there is no any interactions between the adsorbed adsorbate molecules is the assumption of the Langmuir isotherm model. Based on this assumption,

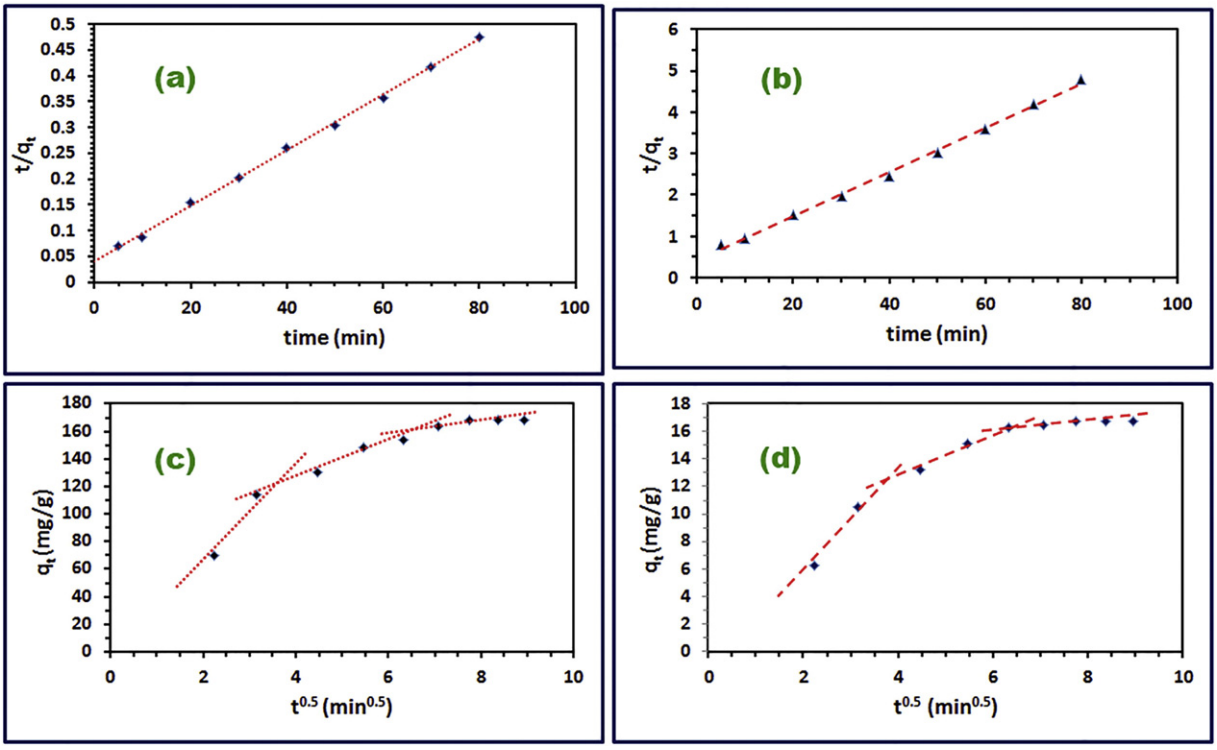

Fig. 11. Adsorption kinetic; pseudo-second-order (a) and intra-particle diffusion model (c) for RR195 dye adsorption; pseudo-second-order (b) and intra-particle diffusion model (d) for OG dye, using MgO nanostructure as an adsorbent.

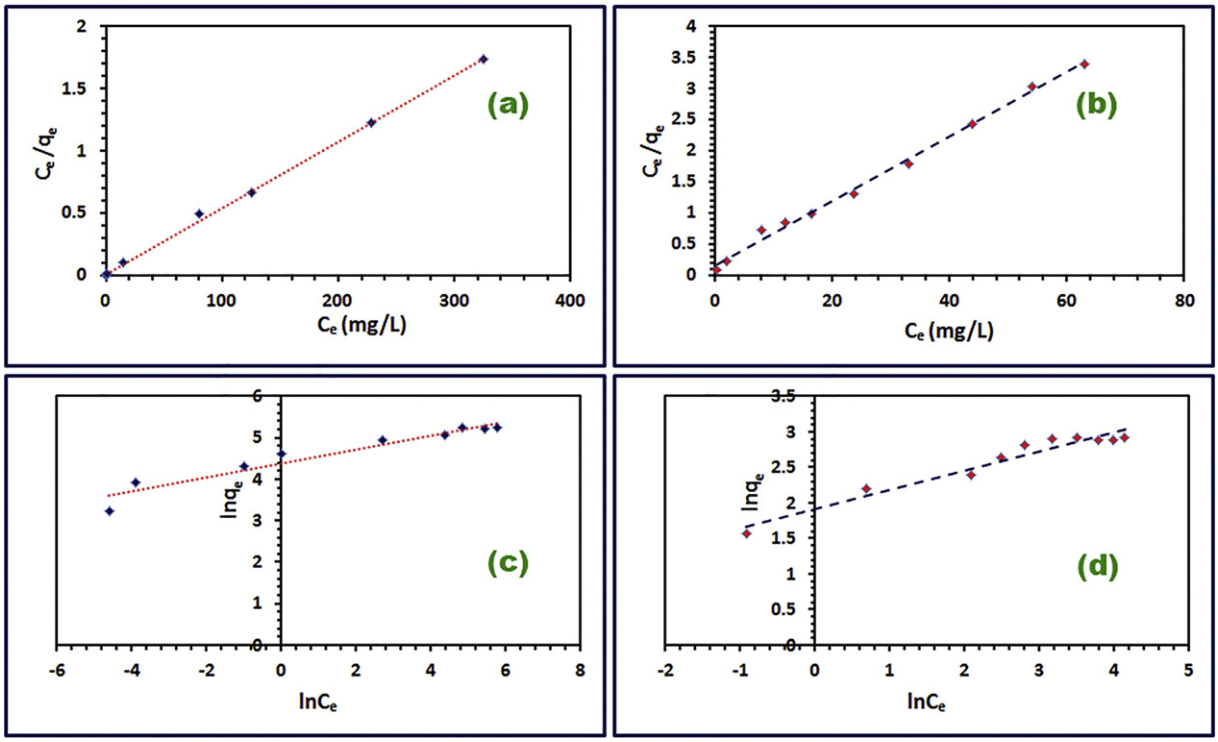

Fig. 12. Langmuir (a) and Freundlich (c) isotherms for RR195 dye adsorption, and Langmuir (b) and Freundlich (d) isotherms for OG dye adsorption, using MgO nanostructure as an adsorbent.

the linearized form of Langmuir isotherm model can be presented as given in Eq. (12) [56].

$$\frac{C_e}{q_e} = \frac{1}{K_L q_m} + \frac{C_e}{q_m} \tag{12}$$

where, C_e is the equilibrium concentration of the dye solution (mg/L), the q_m constant is the maximum adsorption capacity (mg/g), and K_L is Langmuir constant (L/mg). The plot of C_e/q_e against C_e values for the adsorption of the dyes results in a straight line for each dye (Fig. 12(a,b)), and the K_L and q_m values (Table 2) can be determined from the intercept and slope of the plots. Additionally, using a dimensionless constant called equilibrium parameter R_L (Eq. (13)), the efficiency and characteristics of the Langmuir isotherm model can be evaluated and presented in Table 2.

$$R_L = \frac{1}{1 + K_L C_o} \tag{13}$$

where, K_L (L/mg) is the Langmuir constant and C_0 (mg/L) is the initial concentrations of the used dyes, and R_L value gives an indication of the nature of the adsorption process whether this process is unfavorable ($R_L > 1$), linear ($R_L = 1$), favorable ($0 < R_L < 1$), or irreversible ($R_L = 0$) [2]. Table 2 exhibits that R_L values lie between zero and one, and this means that the adsorption of the RR195 and OG dyes, separately, on MgO adsorbent is favorable.

On the other hand, the linearized form of the Freundlich isotherm model based on the assumption that the adsorption takes place on a heterogeneous surface can be given by Eq. (14) [56].

$$\ln q_e = \ln K_F + \frac{1}{n} \ln C_e \tag{14}$$

where, C_e, K_F, and 1/n are the equilibrium concentration of the dyes (mg/L), the Freundlich constant [(mg/g)(L/mg)$^{1/n}$], and the heterogeneity factor which indicates the adsorption strength [56], respectively. The values of K_F and 1/n can be calculated from the slope and intercept of the linear plot of $\ln q_e$ against $\ln C_e$ (Fig. 12(c,d)). The value of 1/n (0–1) can be used as an indication of the surface heterogeneity, and the closer the value to zero the higher the heterogeneity [55–58]. Based on the parameters estimated using the Freundlich isotherm model (Table 2), it could be concluded that the adsorption of the dyes of interest on MgO adsorbent took place on a heterogeneous surface since the 1/n value was in the range of 0–1. Moreover, the maximum adsorption capacity, $q_{m(cal)}$ (as presented in Table 2), can also be estimated employing the Freundlich isotherm model by using Eq. (15) as reported by Halsey [59].

$$K_F = \frac{q_m}{C_0^{1/n}} \tag{15}$$

The calculated isothermal constants (Table 2) lead us to conclude that the adsorption of the RR195 and OG dyes on MgO adsorbent fits better the Langmuir isotherm model. Moreover, the adsorption is a monolayer coverage because the correlation coefficient (r^2) values are closer to unity, and the $q_{m(cal)}$ values are closer to the experimental

Table 2
Langmuir and Freundlich isotherm parameters for the adsorption of RR195 and OG dyes on MgO adsorbent.

Adsorption isotherm model	Constants	RR195 dye Value	OG dye Value
Langmuir	K_L (L/mg)	0.379	0.343
	$q_{m(cal)}$ (mg/g)	187.8	19.27
	r_1^2	0.999	0.995
	R_L	0.36–0.05	0.028–0.226
	$q_{m(exp)}$ (mg/g)	186.1	18.1
	K_F [(mg/g)(L/mg)$^{1/n}$]	80.22	6.826
Freundlich	$q_{m(cal)}$ (mg/g)	80.22	6.826
	r_2^2	0.929	0.946
	n	5.9	3.72
	$q_{m(exp)}$ (mg/g)	186.1	18.1

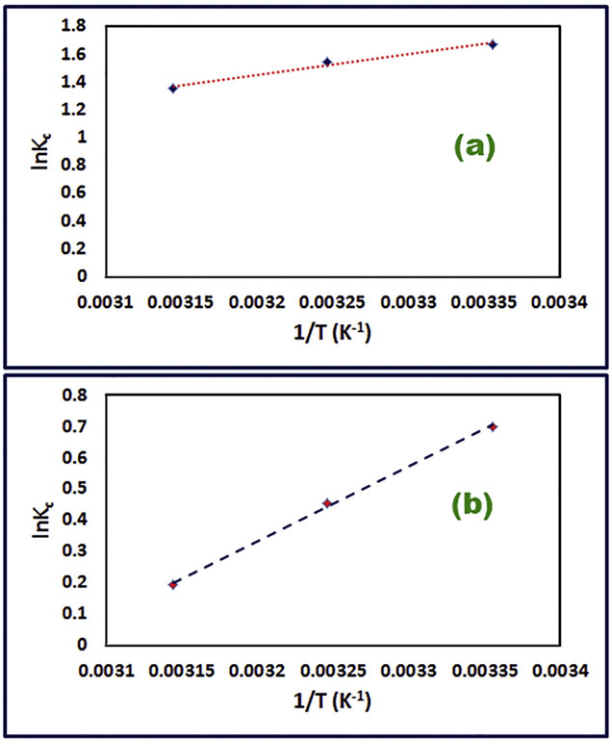

Fig. 13. Plot of ln K_c against 1/T for the adsorption of RR195 dye (a) and OG dye (b) on MgO nano-adsorbent.

ones on comparing to those calculated from the Freundlich isotherm model.

3.2.8. Thermodynamic studies

In order to determine some thermodynamic parameters such as a change in enthalpy (ΔH^0), change in free energy (ΔG^0), and change in the entropy (ΔS^0) employing Eqs. (16) and (17) [2,60], some batch experiments were performed at different temperatures: 298, 308, and 318 K.

$$\ln K_c = \frac{\Delta S^0}{R} - \frac{\Delta H^0}{RT} \quad (16)$$

$$\Delta G = \Delta H - T\Delta S^0 \quad (17)$$

where, K_c, T, and R are the thermodynamic equilibrium constant (L/g) which can be calculated from the relationship ($K_c = q_e/C_e$), universal gas constant (8.314×10^{-3} kJ/mol.K), and absolute temperature (K) of the adsorption media, respectively. The Van't Hoff plot (Eq. (16), Fig. 13) results in a straight line, and ΔH^0 and ΔS^0 constants can be determined from the slope and intercept of the obtained straight line (Table 3). Furthermore, feeding Eq. (17) with ΔH^0 and ΔS^0 values generates ΔG^0 value (Table 3). It is clearly seen from Table 3 that the adsorption of RR195 and OG dyes on the as-prepared MgO nano-adsorbent is spontaneous and exothermic process due to the obtained negative ΔG^0 and ΔH^0 values for this process, respectively. Besides,

Table 3
Thermodynamic parameters for the adsorption of RR195 and OG dyes on MgO adsorbent.

Temperature (K)	RR195 dye			OG dye		
	ΔG^0 (kJ/mol)	ΔS^0 (J/mol.K)	ΔH^0 (kJ/mol)	ΔG^0 (kJ/mol)	ΔS^0 (J/mol.K)	ΔH^0 (kJ/mol)
298	−4.179	−0.0279	−12.486	−1.746	−0.0611	−19.939
308	−3.899			−1.136		
318	−3.621			−0.525		

Table 4
Effects of fuel and crystallite size on the maximum adsorption capacity (q_m) of MgO products for the removal of RR195 and OG dyes.

Fuel	Sample	Crystallite size (nm)	q_m(mg/g)	
			RR195 dye	OG dye
Urea	A_{550}	30	192.9	19.3
	A_{800}	90	161.2	11.8
Oxalic acid	B_{550}	12	207	21.5
	B_{800}	51	186	18.1
Citric acid	C_{550}	–	–	–
	C_{800}	79	173	16.5

reducing the negative values of ΔG^0 on raising the temperature indicates that the adsorption process is less favored at higher temperatures. Moreover, the adsorption of both dyes on the as-prepared nano-adsorbent is physisorption because the ΔH^0 values are <40 kJ/mol and the ΔG^0 values are between −20 and 0 kJ/mol [23].

3.2.9. Influence of the used fuels on the adsorption process

The effect of the used fuel on the adsorption process has been investigated by applying the previously obtained optimum adsorption conditions to calculate the maximum adsorption capacities of the various MgO products synthesized using different fuels calcined at different calcination temperatures (Table 4 and Fig. 14). The results revealed that oxalic acid fuel produced MgO product (B_{550}) with the smallest crystallite size, and this product had the highest adsorption capacities; 207 and 21.5 mg/g for the removal of RR195 and OG dyes respectively. Moreover, increasing the calcination temperatures enhances the crystallite size; consequently, this reduces the adsorption capacity and so that the sample A_{800} has the smallest adsorption capacity.

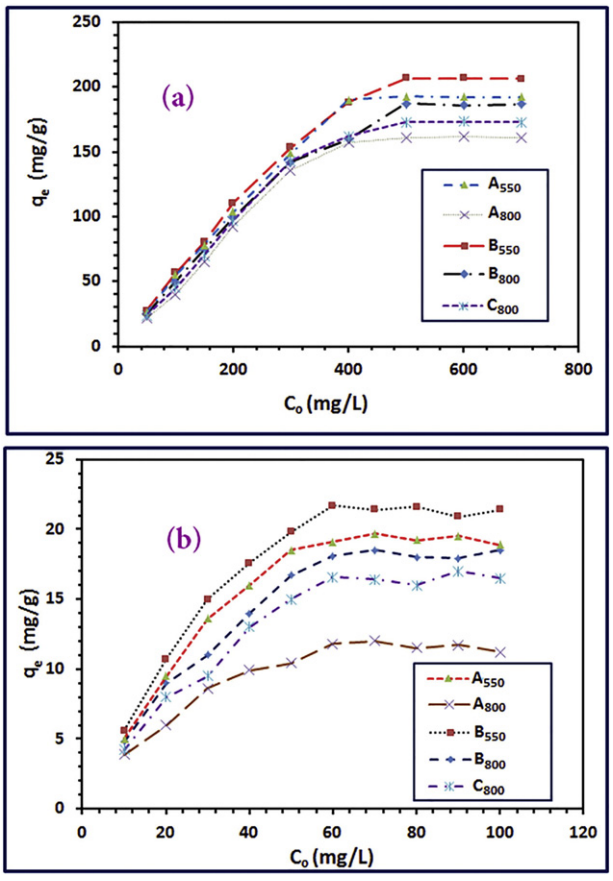

Fig. 14. Effects of fuel and crystallite size on the maximum adsorption capacity (q_m) of MgO products at different initial dye concentration of RR195 (a) and OG (b) dyes.

Table 5
Comparison of adsorption capacities with different adsorbents for the removal of RR195 dye.

Adsorbent material	Adsorption capacities, q_m, mg/g	Refs.
Cone biomass	7.38	[61]
α-Fe_2O_3	20.5	[2]
Modified palygorskite with 3-aminopropyl triethoxysilane	34.24	[62]
Dehydrated beet pulp carbon	58.0	[63]
TiO_2	87	[64]
$CoFe_2O_4$	91.7	[46]
Wheat bran	119.1	[65]
MgO nanoparticles	207	Present study

3.2.10. Comparison of MgO adsorbent efficiency with other adsorbents

Finally, Tables 5 and 6 compared between maximum adsorption capacities (q_m) for the adsorption of RR195 and OG dyes, respectively, on MgO nano-adsorbent with other reported adsorbents. Table 5 reveals that the as-prepared MgO adsorbent has the highest removal efficiency in comparison to the tabulated adsorbents for the removal of RR195 dye from aqueous media. On the other hand, it is clearly obvious that the as-prepared MgO adsorbent has the relatively higher q_m values compared to most of the tabulated adsorbents for the removal of OG dye, as shown in Table 6. Hence, our simple preparation and this comparison suggest that the as-prepared MgO may be applicable and promising in wastewater treatment.

4. Conclusions

Magnesium oxide nanostructures were successfully prepared employing a hybrid sol-gel combustion method using various fuels such as urea, oxalic acid, and citric acid. The results showed that the fuel type had a significant effect on the as-prepared products including identity, crystallite size and morphology. The oxalic acid fuel produced pure MgO nanoparticles with the smallest crystallite size (ca. 12 nm). The prepared MgO nanostructures have high adsorption capacity for the removal of textile anionic dyes such as Reactive Red 195 (RR195) and Orange G (OG). The results revealed that MgO nanostructure generated from the oxalic acid fuel has the highest adsorption capacity 207 and 21.5 mg/g for RR195 and OG dyes respectively. Besides, the adsorption results fitted well the pseudo-second-order model and Langmuir adsorption isotherm model. Additionally, the adsorption mechanism was not controlled only by intra-particle diffusion mechanism but also controlled by bulk diffusion and film diffusion mechanisms. Moreover, the adsorption of the textile dyes on the as-prepared MgO nanostructures was an exothermic, physisorption, and spontaneous process.

Acknowledgements

The authors thank Benha University, Egypt, for the financial support of the current research.

Table 6
Comparison of adsorption capacities with different adsorbents for the removal of OG dye.

Adsorbent material	Adsorption capacities, q_m, mg/g	Refs.
Hematite	0.63	[66]
Modified sawdust	5.48	[67]
MgO nanoparticles	21.5	This study
Magnetic biochar	32.36	[68]
Mesoporous carbon CMK-3	189	[69]

References

[1] T.A. Khan, S. Dahiya, I. Ali, Use of kaolinite as adsorbent: equilibrium, dynamics and thermodynamic studies on the adsorption of Rhodamine B from aqueous solution, Appl. Clay Sci. 69 (2012) 58–66.
[2] M.Y. Nassar, I.S. Ahmed, T.Y. Mohamed, M. Khatab, A controlled, template-free, and hydrothermal synthesis route to sphere-like [small alpha]-Fe_2O_3 nanostructures for textile dye removal, RSC Adv. 6 (2016) 20001–20013.
[3] M.Y. Nassar, A.S. Amin, I.S. Ahmed, S. Abdallah, Sphere-like Mn_2O_3 nanoparticles: facile hydrothermal synthesis and adsorption properties, J. Taiwan Inst. Chem. Eng. 64 (2016) 79–88.
[4] W. Wang, T. Jiao, Q. Zhang, X. Luo, J. Hu, Y. Chen, Q. Peng, X. Yan, B. Li, Hydrothermal synthesis of hierarchical core-shell manganese oxide nanocomposites as efficient dye adsorbents for wastewater treatment, RSC Adv. 5 (2015) 56279–56285.
[5] G. Moussavi, M. Mahmoudi, Removal of azo and anthraquinone reactive dyes from industrial wastewaters using MgO nanoparticles, J. Hazard. Mater. 168 (2009) 806–812.
[6] B.K. Körbahti, A. Tanyolaç, Electrochemical treatment of simulated textile wastewater with industrial components and levafix blue CA reactive dye: optimization through response surface methodology, J. Hazard. Mater. 151 (2008) 422–431.
[7] F. Han, V.S.R. Kambala, M. Srinivasan, D. Rajarathnam, R. Naidu, Tailored titanium dioxide photocatalysts for the degradation of organic dyes in wastewater treatment: a review, Appl. Catal. A Gen. 359 (2009) 25–40.
[8] M.A. Mottaleb, D. Littlejohn, Application of an HPLC-FTIR modified thermospray interface for analysis of dye samples, Anal. Sci. 17 (2001) 429–434.
[9] N.F. Cardoso, R.B. Pinto, E.C. Lima, T. Calvete, C.V. Amavisca, B. Royer, M.L. Cunha, T.H.M. Fernandes, I.S. Pinto, Removal of remazol black B textile dye from aqueous solution by adsorption, Desalination 269 (2011) 92–103.
[10] J. Huang, Y. Cao, Z. Liu, Z. Deng, W. Wang, Application of titanate nanoflowers for dye removal: a comparative study with titanate nanotubes and nanowires, Chem. Eng. J. 191 (2012) 38–44.
[11] M.Y. Nassar, I.S. Ahmed, Template-free hydrothermal derived cobalt oxide nanopowders: synthesis, characterization, and removal of organic dyes, Mater. Res. Bull. 47 (2012) 2638–2645.
[12] M.Y. Nassar, I.S. Ahmed, I. Samir, A novel synthetic route for magnesium aluminate ($MgAl_2O_4$) nanoparticles using sol–gel auto combustion method and their photocatalytic properties, Spectrochim. Acta A Mol. Biomol. Spectrosc. 131 (2014) 329–334.
[13] H.R. Mahmoud, S.M. Ibrahim, S.A. El-Molla, Textile dye removal from aqueous solutions using cheap MgO nanomaterials: adsorption kinetics, isotherm studies and thermodynamics, Adv. Powder Technol. 27 (2016) 223–231.
[14] R.G. Saratale, G.D. Saratale, J.S. Chang, S.P. Govindwar, Bacterial decolorization and degradation of azo dyes: a review, J. Taiwan Inst. Chem. Eng. 42 (2011) 138–157.
[15] H.M. Aly, M.E. Moustafa, M.Y. Nassar, E.A. Abdelrahman, Synthesis and characterization of novel Cu (II) complexes with 3-substituted-4-amino-5-mercapto-1,2,4-triazole Schiff bases: a new route to CuO nanoparticles, J. Mol. Struct. 1086 (2015) 223–231.
[16] T.A. Khan, M. Nazir, E.A. Khan, Adsorptive removal of Rhodamine B from textile wastewater using water chestnut (*Trapa natans* L.) peel: adsorption dynamics and kinetic studies, Toxicol. Environ. Chem. 95 (2013) 919–931.
[17] S.D. Khattri, M.K. Singh, Use of sagaun sawdust as an adsorbent for the removal of crystal violet dye from simulated wastewater, Environ. Prog. Sustain. Energy 31 (2012) 435–442.
[18] Y.S. Jeon, J. Lei, J.-H. Kim, Dye adsorption characteristics of alginate/polyaspartate hydrogels, J. Ind. Eng. Chem. 14 (2008) 726–731.
[19] A. Kuleyin, F. Aydin, Removal of reactive textile dyes (remazol brillant blue R and remazol yellow) by surfactant-modified natural zeolite, Environ. Prog. Sustain. Energy 30 (2011) 141–151.
[20] M.Y. Nassar, Size-controlled synthesis of $CoCO_3$ and Co_3O_4 nanoparticles by free-surfactant hydrothermal method, Mater. Lett. 94 (2013) 112–115.
[21] M.Y. Nassar, A.S. Attia, K.A. Alfallous, M.F. El-Shahat, Synthesis of two novel dinuclear molybdenum(0) complexes of quinoxaline-2,3-dione: new precursors for preparation of α-MoO_3 nanoplates, Inorg. Chim. Acta 405 (2013) 362–367.
[22] M.Y. Nassar, T.Y. Mohamed, I.S. Ahmed, One-pot solvothermal synthesis of novel cobalt salicylaldimine–urea complexes: a new approach to Co_3O_4 nanoparticles, J. Mol. Struct. 1050 (2013) 81–87.
[23] M.Y. Nassar, M.M. Moustafa, M.M. Taha, Hydrothermal tuning of the morphology and particle size of hydrozincite nanoparticles using different counterions to produce nanosized ZnO as an efficient adsorbent for textile dye removal, RSC Adv. 6 (2016) 42180–42195.
[24] T. Jiao, Y. Liu, Y. Wu, Q. Zhang, X. Yan, F. Gao, A.J.P. Bauer, J. Liu, T. Zeng, B. Li, Facile and scalable preparation of graphene oxide-based magnetic hybrids for fast and highly efficient removal of organic dyes, Sci. Rep. 5 (2015) 12451.
[25] H. Guo, T. Jiao, Q. Zhang, W. Guo, Q. Peng, X. Yan, Preparation of graphene oxide-based hydrogels as efficient dye adsorbents for wastewater treatment, Nanoscale Res. Lett. 10 (2015) 1–10.
[26] M.Y. Nassar, I.S. Ahmed, Hydrothermal synthesis of cobalt carbonates using different counter ions: an efficient precursor to nano-sized cobalt oxide (Co_3O_4), Polyhedron 30 (2011) 2431–2437.
[27] R. Xing, T. Jiao, Y. Liu, K. Ma, Q. Zou, G. Ma, X. Yan, Co-assembly of graphene oxide and albumin/photosensitizer Nanohybrids towards enhanced photodynamic therapy, Polymer 8 (2016) 181.
[28] R. Xing, K. Liu, T. Jiao, N. Zhang, K. Ma, R. Zhang, Q. Zou, G. Ma, X. Yan, An injectable self-assembling collagen–gold hybrid hydrogel for combinatorial antitumor photothermal/photodynamic therapy, Adv. Mater. 28 (2016) 3669–3676.
[29] A.-N.M. Salem, M.A. Ahmed, M.F. El-Shahat, Selective adsorption of amaranth dye on Fe_3O_4/MgO nanoparticles, J. Mol. Liq. 219 (2016) 780–788.

[30] G. Yuan, J. Zheng, C. Lin, X. Chang, H. Jiang, Electrosynthesis and catalytic properties of magnesium oxide nanocrystals with porous structures, Mater. Chem. Phys. 130 (2011) 387–391.
[31] A. Umar, M.M. Rahman, Y.-B. Hahn, MgO polyhedral nanocages and nanocrystals based glucose biosensor, Electrochem. Commun. 11 (2009) 1353–1357.
[32] K. Zhang, Y. An, L. Zhang, Q. Dong, Preparation of controlled nano-MgO and investigation of its bactericidal properties, Chemosphere 89 (2012) 1414–1418.
[33] S.-H. Chiu, W.-K. Wang, The dynamic flammability and toxicity of magnesium hydroxide filled intumescent fire retardant polypropylene, J. Appl. Polym. Sci. 67 (1998) 989–995.
[34] S. Stankic, M. Müller, O. Diwald, M. Sterrer, E. Knözinger, J. Bernardi, Size-dependent optical properties of MgO nanocubes, Angew. Chem. Int. Ed. 44 (2005) 4917–4920.
[35] P. Jeevanandam, K.J. Klabunde, A study on adsorption of surfactant molecules on magnesium oxide nanocrystals prepared by an aerogel route, Langmuir 18 (2002) 5309–5313.
[36] F. Granados-Correa, J. Bonifacio-Martínez, V.H. Lara, P. Bosch, S. Bulbulian, Cobalt sorption properties of MgO prepared by solution combustion, Appl. Surf. Sci. 254 (2008) 4688–4694.
[37] A.R. Bueno, R.F.M. Oman, P.M. Jardim, N.A. Rey, R.R. de Avillez, Kinetics of nanocrystalline MgO growth by the sol–gel combustion method, Microporous Mesoporous Mater. 185 (2014) 86–91.
[38] J.P. Dhal, M. Sethi, B.G. Mishra, G. Hota, MgO nanomaterials with different morphologies and their sorption capacity for removal of toxic dyes, Mater. Lett. 141 (2015) 267–271.
[39] S. Li, B. Zhou, B. Ren, L. Xing, L. Tan, L. Dong, J. Li, Preparation of MgO nanomaterials by microemulsion-based oil/water interface precipitation, Mater. Lett. 171 (2016) 204–207.
[40] P.B. Devaraja, D.N. Avadhani, S.C. Prashantha, H. Nagabhushana, S.C. Sharma, B.M. Nagabhushana, H.P. Nagaswarupa, Synthesis, structural and luminescence studies of magnesium oxide nanopowder, Spectrochim. Acta A Mol. Biomol. Spectrosc. 118 (2014) 847–851.
[41] S.R. Jain, K.C. Adiga, V.R. Pai Verneker, A new approach to thermochemical calculations of condensed fuel-oxidizer mixtures, Combust. Flame 40 (1981) 71–79.
[42] R. Jenkins, R.L. Snyder, Introduction to X-Ray Powder Diffractometry, John Wiley & Sons, Inc., New York, 1996.
[43] M. Mostafa, H.M. Saber, A.A. El-Sadek, M.Y. Nassar, Preparation and performance of 99Mo/99mTc chromatographic column generator based on zirconium molybdosilicate, Radiochim. Acta. (2016) 257–265.
[44] Y.S. Al-Degs, M.I. El-Barghouthi, A.H. El-Sheikh, G.M. Walker, Effect of solution pH, ionic strength, and temperature on adsorption behavior of reactive dyes on activated carbon, Dyes Pigments 77 (2008) 16–23.
[45] M.Y. Nassar, S. Abdallah, Facile controllable hydrothermal route for porous $CoMn_2O_4$ nanostructure: synthesis, characterization, and textile dye removal from aqueous media, RSC Adv. 6 (2016) 84050–84067.
[46] M.Y. Nassar, M. Khatab, Cobalt ferrite nanoparticles via a template-free hydrothermal route as an efficient nano-adsorbent for potential textile dye removal, RSC Adv. 6 (2016) 79688–79705.
[47] X. Wang, N. Zhu, B. Yin, Preparation of sludge-based activated carbon and its application in dye wastewater treatment, J. Hazard. Mater. 153 (2008) 22–27.
[48] F.A. Pavan, S.L.P. Dias, E.C. Lima, E.V. Benvenutti, Removal of Congo red from aqueous solution by anilinepropylsilica xerogel, Dyes Pigments 76 (2008) 64–69.
[49] T.G. Venkatesha, R. Viswanatha, Y. Arthoba Nayaka, B.K. Chethana, Kinetics and thermodynamics of reactive and vat dyes adsorption on MgO nanoparticles, Chem. Eng. J. 198–199 (2012) 1–10.
[50] G. Alberghina, R. Bianchini, M. Fichera, S. Fisichella, Dimerization of cibacron blue F_3GA and other dyes: influence of salts and temperature, Dyes Pigments 46 (2000) 129–137.
[51] D. Hu, L. Wang, Adsorption of amoxicillin onto quaternized cellulose from flax noil: kinetic, equilibrium and thermodynamic study, J. Taiwan Inst. Chem. Eng. 64 (2016) 227–234.
[52] W.J. Wber, J.C. Morris, Proceedings of the International Conference on Water Pollution Symposium, Pergamon Press, Oxford; New York, 1962.
[53] F.A. Batzias, D.K. Sidiras, Dye adsorption by prehydrolysed beech sawdust in batch and fixed-bed systems, Bioresour. Technol. 98 (2007) 1208–1217.
[54] C. Luo, Z. Tian, B. Yang, L. Zhang, S. Yan, Manganese dioxide/iron oxide/acid oxidized multi-walled carbon nanotube magnetic nanocomposite for enhanced hexavalent chromium removal, Chem. Eng. J. 234 (2013) 256–265.
[55] K.Y. Foo, B.H. Hameed, Insights into the modeling of adsorption isotherm systems, Chem. Eng. J. 156 (2010) 2–10.
[56] C. Muthukumaran, V.M. Sivakumar, M. Thirumarimurugan, Adsorption isotherms and kinetic studies of crystal violet dye removal from aqueous solution using surfactant modified magnetic nanoadsorbent, J. Taiwan Inst. Chem. Eng. 63 (2016) 354–362.
[57] S. Agarwal, I. Tyagi, V.K. Gupta, F. Golbaz, A.N. Golikand, O. Moradi, Synthesis and characteristics of polyaniline/zirconium oxide conductive nanocomposite for dye adsorption application, J. Mol. Liq. 218 (2016) 494–498.
[58] V.S. Munagapati, D.-S. Kim, Adsorption of anionic azo dye congo red from aqueous solution by cationic modified orange peel powder, J. Mol. Liq. 220 (2016) 540–548.
[59] G.D. Halsey, The role of surface heterogeneity in adsorption, in: V.I.K.W.G. Frankenburg, E.K. Rideal (Eds.), Advances in Catalysis, Academic Press 1952, pp. 259–269.
[60] S. Liu, Y. Ding, P. Li, K. Diao, X. Tan, F. Lei, Y. Zhan, Q. Li, B. Huang, Z. Huang, Adsorption of the anionic dye congo red from aqueous solution onto natural zeolites modified with *N*,*N*-dimethyl dehydroabietylamine oxide, Chem. Eng. J. 248 (2014) 135–144.
[61] O. Aksakal, H. Ucun, Equilibrium, kinetic and thermodynamic studies of the biosorption of textile dye (Reactive Red 195) onto *Pinus sylvestris* L, J. Hazard. Mater. 181 (2010) 666–672.
[62] A. Xue, S. Zhou, Y. Zhao, X. Lu, P. Han, Adsorption of reactive dyes from aqueous solution by silylated palygorskite, Appl. Clay Sci. 48 (2010) 638–640.
[63] A.Y. Dursun, O. Tepe, Removal of Chemazol Reactive Red 195 from aqueous solution by dehydrated beet pulp carbon, J. Hazard. Mater. 194 (2011) 303–311.
[64] V. Belessi, G. Romanos, N. Boukos, D. Lambropoulou, C. Trapalis, Removal of Reactive Red 195 from aqueous solutions by adsorption on the surface of TiO_2 nanoparticles, J. Hazard. Mater. 170 (2009) 836–844.
[65] F. Çiçek, D. Özer, A. Özer, A. Özer, Low cost removal of reactive dyes using wheat bran, J. Hazard. Mater. 146 (2007) 408–416.
[66] M.K. Mondal, S. Singh, M. Umareddy, B. Dasgupta, Removal of Orange G from aqueous solution by hematite: isotherm and mass transfer studies, Korean J. Chem. Eng. 27 (2010) 1811–1815.
[67] S. Banerjee, M.C. Chattopadhyaya, Y. Chandra Sharma, Removal of an azo dye (Orange G) from aqueous solution using modified sawdust, J Water Sanit. Hyg. Dev. 5 (2015) 235–243.
[68] N.M. Mubarak, Y.T. Fo, H.S. Al-Salim, J.N. Sahu, E.C. Abdullah, S. Nizamuddin, N.S. Jayakumar, P. Ganesan, Removal of methylene blue and Orange-G from waste water using magnetic biochar, Int. J. Nanosci. 14 (2015) 1550009.
[69] B.G.A.K. Arzani, A.H.A. Kashi, Equilibrium and kinetic adsorption study of the removal of Orange-G dye using carbon mesoporous material, J. Inorg. Mater. 27 (2012) 660–666.